Actuator Load Estimation From Distributed Optical Sensing of Airframe Deformation

Actuator Load Estimation From Distributed Optical Sensing of Airframe Deformation

Gaetano Quattrocchi

Department of Mechanics and Aerospace, Politecnico di Torino, Italy. E-mail: gaetano.quattrocchi@polito.it

Pier Carlo Berri

Department of Mechanics and Aerospace, Politecnico di Torino, Italy. E-mail: piercarlo.berri@polito.it

Matteo Davide Lorenzo Dalla Vedova

Department of Mechanics and Aerospace, Politecnico di Torino, Italy. E-mail: matteo.dallavedova@polito.it

Paolo Maggiore

Department of Mechanics and Aerospace, Politecnico di Torino, Italy. E-mail: paolo.maggiore@polito.it

Real-time health monitoring of flight control actuators usually involves the comparison of measured signals either with numerical models or with statistical data. As the external loads experienced by the system influence the operation of most actuators, such loads are a useful quantity to compare with the actuator output and perform on-board fault detection. In common flight controls, the actuator load is not directly available as a measured signal, due to the reliability and complexity penalties often associated to the installation of dedicated sensors and transducers. In this work, we discuss the use of distributed sensing of the airframe strain to infer the aerodynamic loads acting on the flight control actuator. We address a specific sensing technology based on Fiber Bragg Gratings (FBGs) as it combines a good accuracy with minimal invasivity and low complexity. Specifically, we combined a structural and an aerodynamic model to collect a database to train data-driven surrogates intended to map from strain measures to actuator load. Figure 1 displays the information flow of the proposed process.

Keywords: distributed optical sensing, FBG, load estimation, on-board fault detection, prognostics.

1. Introduction

The idea of a fiber-optic structural monitoring system arises from the cost considerations associated with the maintenance of an aircraft during its life cycle. Maintenance, especially structural monitoring based on periodic checks is an important expenditure item for airlines (Dupuy et al., 2011).

Currently, the techniques for structural monitoring consist of non-destructive methods (Kamsu-Foguem, 2012), which however are limited by the accessibility to the area of interest of the components to be inspected. Furthermore, these techniques are often very expensive due to the high workload required (Qing et al., 2005). It is therefore evident that the use of an integrated system for structural monitoring, possibly capable of processing data in real time, is considerably advantageous, even in terms of cost (Dong and Kim, 2018). Generally, traditional strain gauge sensors are used, i.e. piezoelectric or ultrasonic sensors which however require dedicated and heavy wiring and are subject to various problems.

Fiber optic technology, on the other hand, has great potential in the aerospace field where phenomena such as fatigue, corrosion, damage impact and overall structural aging are significant and difficult to control issues. Furthermore, the increasing use of composite materials leads to the need to investigate and prevent new phenomena such as delamination and, in general, the various failure mechanisms which in composites are extremely complex and unpredictable (Jones, 1998). The possibility of integrating the monitoring system within the components themselves (between the lamination layers or in the matrix, such as in Melnykowycz et al. (2006)) is therefore a further important advantage.

In summary, an integrated monitoring system has the following advantages:

(a) Maintenance costs reduction.

(b) Reduction of maintenance times.

(c) Ability to locate damage and, ideally, real time addressing strategies.

(d) Ability to organize the maintenance plan based on the actual health state of the monitored components.

Proceedings of the 31st European Safety and Reliability Conference
Edited by Bruno Castanier, Marko Cepin, David Bigaud, and Christophe Berenguer
Published by Research Publishing, Singapore.
ISBN: 978-981-18-2016-8; doi:10.3850/978-981-18-2016-8_564-cd

(e) Ability to collect real-time data on the structure, useful for various functions (e.g. prognostics, performance optimization).

In this context, this work is an expression of this paradigm of real-time monitoring.

2. Scope of the work

The scope of the work is to present a novel method to evaluate, in real-time, the hinge moment of an aircraft aileron. Complete workflow can be found in Figure 1.

Two main branches are visible: offline computing and real-time monitoring. Most of the work is relative to the offline process, where a suitable surrogate model has to be generated using numerical data obtained via simulations of various flight conditions.

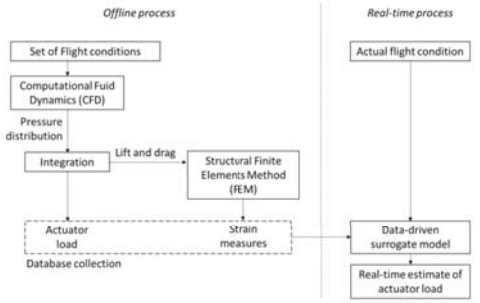

Fig. 1. Process overview.

In particular, a database of CFD (Computational Fluid Dynamics) and FEM (Finite Elements Method) simulation has to be created, in order to obtain aerodynamic loads and structure deformation, respectively. In fact, the pressure field obtained for a given set of operating conditions using CFD, is used as external load for FEM analyses, and also the pressure distribution on the control surface is integrated to calculate the force acting on the servoactuator.

Another important step is to evaluate the placement of FBG (Fiber Bragg Gratings) optical sensors, whose scope is to sense the deformation at a particular spatial point (Ma and Chen, 2019) - this concept has been already explored in Berri et al. (2020); all of these measurements are used as input for an ANN (Artificial Neural Network), including other relevant data such as atmospheric data and attitude information obtained by other on-board instruments. In this sense, this is a sensor-fusion approach.

After proper training, leveraging a supervised learning approach, the network output is the aileron hinge moment, obtained using real-time flight conditions.

Given the complexity of the approach, in this paper only the first part of the algorithm will be explored, i.e. databases generation and sensors placement.

3. Model definition

The aircraft used in this work is an electric, solar-powered UAV (Unmanned Aerial Vehicle), RA, conceptualized and designed (Fig. 2) by students team Icarus at Politecnico di Torino.

The vehicle adopts a conventional high wing configuration, with a 5 m wingspan. Fuselage is bubble shaped, with a length of 2m; the tail is T-shaped, with 0.5m height. Propulsion is achieved using a single 50 cm propeller placed in the front of the fuselage, actuated by one electric motor. External surfaces and main structural components are made using composite materials.

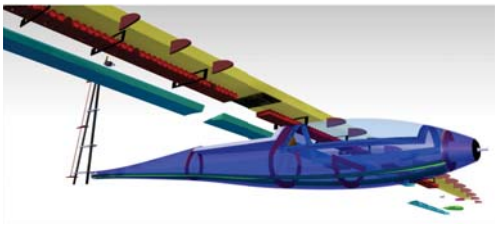

Fig. 2. Prototype CAD design.

In this work, the focus will be on the aircraft wing, which will now be briefly described.

In Fig. 3 a CAD model of the wing is shown. The battery pack (red), used for energy storage, is placed inside the wing in order to maximize the roll moment of inertia of the aircraft and thus increasing the response time of the aircraft along that axis improving controllability. In the main structure, three main elements are visible (ref. Figure 3):

(a) Skin (light blue), made of laminated carbon fiber (two layers at $\pm 45°$) , which holds the aerodynamic shape;

(b) Wingbox (yellow), made of laminated carbon fiber (two layers at $\pm 90°$), that is the main load-bearing component;

(c) Ribs (gray), made of sandwich composite, with the faces made of three layers of laminated carbon fiber and core in Roahcell, used for longitudinal strengthening and skin shaping.

Geometrical details can be found in Table 1 and Figure 4, while aerodynamics data are reported in Table 2.

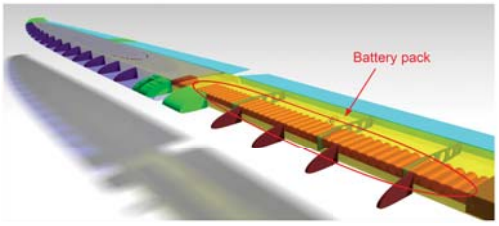

Fig. 3. CAD detail of wing structure.

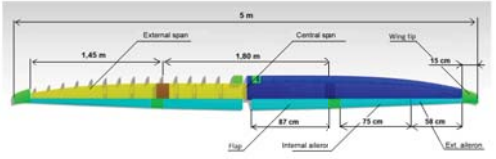

Fig. 4. CAD schematics of wing (top view)

Table 1. Relevant wing geometrical data

Root chord	0.340 m
Tip chord	0.080 m
Wingspan	5 m
Wing surface	1.356 m^2
Aspect Ratio	18.5

4. Flight conditions

All analysis will be carried out considering ISA standard atmospheric conditions, i.e. $p = 1.01 \cdot 10^5\ Pa$, $T = 15$ °C, considering also zero altitude, i.e. $\rho = 1.225\ kg/m^3$.

Regarding ranges for angle of attack α and speed V, it was decided to analyze values around nominal flight conditions ($V = 15\ m/s$, $\alpha = 3.5°$). Thus, combinations of the following values will be considered: $V = [10, 15, 20]\ m/s$, $\alpha = [2, 5, 8]°$.

As reported in Belelli (2020) and Frediani (2020), the key requirements to comply with the imposed mission profile are $V = 15\ m/s$, turn radius $R = 100\ m$ and maneuver time $t_m = 0.25\ s$. Thus, the study shows that maximum aileron deflection angle required is $\delta_a = 18°$; in any case, the model is designed to have an actuation range of $\delta_a = \pm 20°$.

Table 2. Relevant wing aerodynamics data for $V_\infty = 15$ m/s

C_{L_0}	0.34
$C_{L_{max}}$	1.5
C_{L_α}	5.58
C_{D_0}	0.011
$C_{D_{min}}$	0.010
C_{M_0}	-0.20
$(C_L/C_D)_{max}$	40

It can be noted that most conditions, as previously stated, are proximal to nominal flight conditions. The total number of combinations simulated is 41, distributed as described, in condensed form, below.

(1) $V = 15\ m/s$
  (a) $\alpha = 2° \ : \ \delta_a = [0, \pm 5, \pm 10, \pm 15, \pm 20]°$;
  (b) $\alpha = [5, 8]° \ : \ \delta_a = [0, \pm 5, \pm 10, \pm 15]°$;

(2) $V = [5, 10]\ m/s$
  (a) $\alpha = [2, 5, 8]° \ : \ \delta_a = [0, \pm 5]°$;

5. CFD analysis

After creating a suitable number of conditions, the following step is to analyze the stress field on the wing. In order to do so, CFD analysis will be carried out firstly to evaluate the pressure field on the wing and thus the distributed load acting on it; at the same time, the integration of the pressure field, limited to the aileron surface, will give an estimation of the load acting on the relative actuator.

All CFD simulations are carried out using Siemens Star-CCM+.

5.1. *Mesh*

The total computation domain is a hemisphere, encompassing half of the vehicle along the longitudinal axis, in order to leverage the symmetry condition, of radius $R_d = 20\ m$, which is 8x the wing span.

The mesh is based on polyhedral cells, which have more interfaces compared to traditional cells; this feature is useful when the flow field is not entirely clear. In general, in presence of a complex flow field, polyhedral cells show better residual at convergence and require less iterations, thus saving computation time (Katz and Sankaran, 2011).

Cell size is variable, as visible in Fig.5, with smaller size in proximity of the profile itself; furthermore an inflation layer is present on the profile itself, composed by 25 prism cell stacked normally to the boundary. The scope of these layers is to effectively capture the boundary layer.

5.2. *Model description*

Regarding boundary conditions, a *free stream* condition is imposed along the external boundary of the computation domain; as previously stated, a

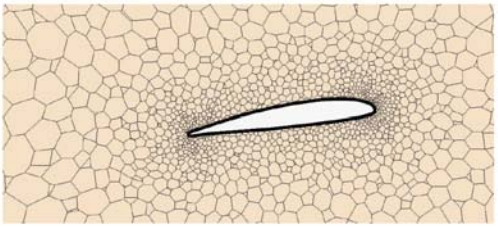

Fig. 5. CFD mesh detail.

simmetry condition is imposed along the longitudinal plane to simplify calculation; finally, a *wall* condition is imposed on all vehicle surfaces.

In setting up the problem, a RANS (Reynolds Averaged Navier Stokes) approach is chosen, since a steady state condition is of interest. The model used takes into account compressibility and turbulence.

In particular, the formulation adopted for turbulence is SST $k-\omega$ with $\gamma - Re_\theta$ transition, which is an hybrid method that uses different equations depending on wall distance (Shah et al., 2015).

5.3. *Results*

Some results, for different conditions, are visible in Fig. 6 and in Fig. 7.

In any case, a csv file is saved for each simulation with the pressure distribution on all surfaces; in particular, such values are absolute static pressures.

These values will now be used in the FEM analysis as distributed loads along the wing.

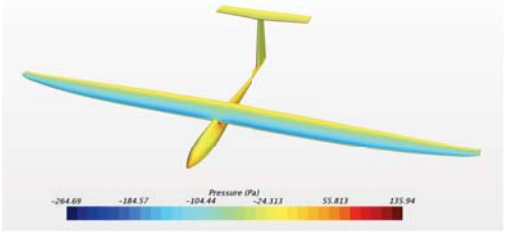

Fig. 6. Vehicle pressure field (relative) in cruise conditions ($V = 15\ m/s,\ \alpha = 2^o,\ \delta_a = 0^o$).

6. FEM analysis

Now that the pressure field around the wing is determined, FEM analysis can be carried out to evaluate the stress state of the wing components. For all analysis the Von Mises criterion will be used.

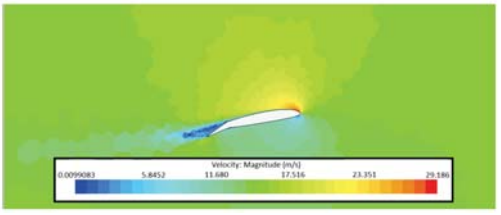

Fig. 7. Wing velocity profile ($V = 15\ m/s,\ \alpha = 2^o,\ \delta_a = 20^o$).

For all simulations, the software suite Altair Hyperworks will be used. In particular, Hypermesh is used for meshing, materials and loads definition, Optistruct is the numerical solver and Hyperview is the post-processing tool.

Before proceeding with FEM analysis, the model has been suitably simplified, removing all non relevant structural elements; furthermore, the mobile surfaces have been removed, while the resulting load on the actuators have been calculated and will be then applied as concentrated loads.

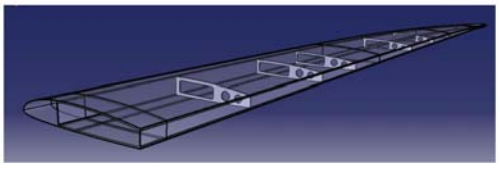

Fig. 8. CAD model simplified for FEM analysis.

6.1. *Meshing*

The minimal size of each element is set as $3\ mm$. The elements used to create the mesh are both *QUAD* elements, for generally flat regions and *TRIA* elements for high curvature zones.

A *biasing* function is used to automatically determine the best element size while keeping a satisfactory quality index, especially in high curvature zones such as the leading edge.

Fig. 9. Skin meshing detail.

6.2. *Materials*

The carbon fabric used for all elements is TeXtreme Carbon Fabric $80\ g/m^2$, (Fig. 10), with the

following mechanical properties: $E = 240\ GPa$, $\sigma_{break} = 4.8GPa$, $\rho = 1.79\ g/cm^3$, $d = 7\ \mu m$, where d is the fiber diameter.

Fig. 10. TeXtreme Fabric.

To create the composite material, the epoxy resin SX10 will be used, in 40% matrix to 60% fiber ratio. Using the Multiscale Designer tool, the following properties are calculated: $E_x = 85\ GPa$, $E_y = 85\ GPa$, $G_{xy} = 11.56\ GPa$, $\nu_{xy} = 4.27 \cdot 10^{-3}$, $\rho = 1.55 \cdot 10^{-3}\ g/mm^3$, where E is the elasticity modulus, G is the shear modulus, ν is the Poisson ratio and ρ is the density.

Furthermore, the number of layers and orientation have to be defined for each laminate. The following scheme will be used:

(1) Skin: two layers at $\pm 45^o$

(2) Wingbox: two layers at $\pm 90^o$

(3) Ribs: eight layers, four at $+45^o$ and four at -45^o.

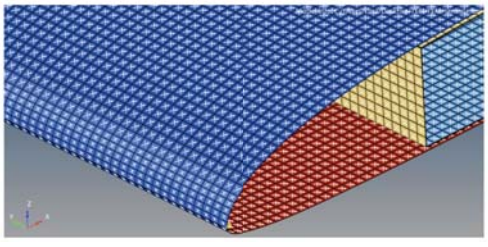

Fig. 11. Mesh detail with materials applied.

6.3. *Constraints and loads*

The structure is constrained, for all six degrees of freedom, on all nodes on contact with the symmetry plane.

Two types of loads are applied to the structure: aerodynamic and inertial loads. Aerodynamic loads have been previously determine in the CFD analysis.

To apply the pressure field to the structure, the *field* function has been used, which maps the loads to each element of the structure.

As previously stated, the concentrated loads acting on the aileron actuators have been calculated and applied. These values have been determined via integration of the pressure field on the aileron surface, thus obtaining the hinge moment and the the two forces acting along x and y direction, since the actuation rod is assumed to be infinitely rigid. In Fig. 12 all applied aerodynamic loads for $V = 15\ m/s,\ \alpha = 2^o,\ \delta_a = -20^o$ are visible.

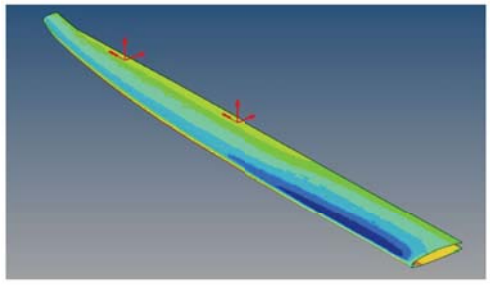

Fig. 12. Aerodynamic loads applied.

As for inertial loads, the solver automatically calculate and distribute the weight of structural elements. Thus, only the battery pack wight has to be manually included in the computation.

The two battery packs have been modeled using distributed loads, of $2.5\ kg/m$ for the internal one (800 mm length, 40 batteries) and $1.625\ kg/m$ for the external one (650 mm length, 32 batteries).

In Fig.5 all loads acting on the wing are visible (the blue arrows represent the mass loads of the battery packs) for the condition $V = 15\ m/s,\ \alpha = 2^o$.

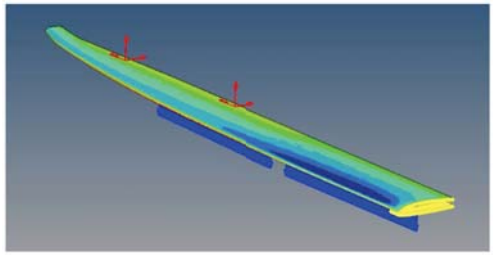

Fig. 13. Schematics of all loads acting on the wing.

6.4. *Results*

The system is now solved to evaluate deformations (as visible in Fig. 14) and strains of the whole structure. All the results have been logged as *csv* files for each simulation.

In particular, the strain values will later be used as basis of the algorithm that evaluate the best placement of the FBG sensors.

Fig. 14. Wing displacement in cruise conditions.

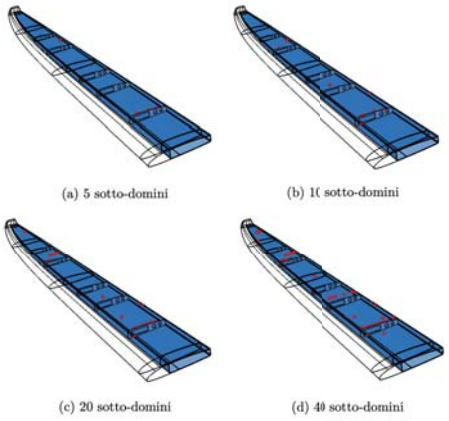

Fig. 15. FBGs identified locations.

The final sensors configuration is shown in Fig. 16.

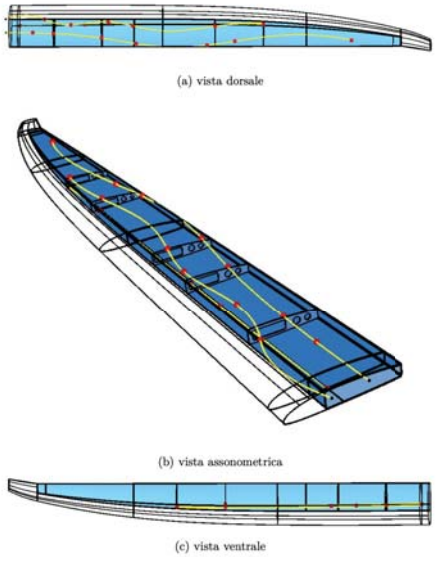

Fig. 16. Final fibers configuration.

7. Sensors configuration

It is now possible to evaluate the best placement for the optical sensors, given the knowledge of the wing stress map in various flight conditions.

The criterion adopted for optimal placement is relatively simple: the sensors will be placed in the spots where the most variability in stresses is present at varying conditions. Using said approach, one can be sure to have the highest stress delta and thus the maximum information gain.

Furthermore, other requirements have been considered, including: hinge moment sensitivity, torsion sensitivity, structural strength, optical signal attenuation (prevention of sharp turns), monitoring system reliability.

The evaluation procedure has been automated using a MATLAB® script, that will evaluate the stress variation for each subdomain across all simulations carried out.

Depending on the number of considered sensors, several configurations are possible. A few are shown in Fig.15.

The optical interrogator used to poll the FBGs (SmartScan SBI) supports up to 64 different FBGs distributed along 4 optical lines; for the final configuration, a three lines setup has been chosen, with 7 and 2x6, for a total of 19 sensors. The fourth line will be used for thermal compensation.

As previously stated, one of the requirements is to have a high degree of system reliability. Thus, a number of sensors lower than the maximum supported is chosen. Furthermore, additional sensors would marginally improve system capabilities given the modest stress variability in such locations.

8. Conclusions and future works

In this work, a preliminary analysis on optimal optical sensors placement for hinge moment determination has been described. The method can be summarized as:

(1) Aerodynamic loads evaluation using CFD analysis:

(2) Structure elastic response determination, considering previously calculated aerodynamic loads, using FEM;

(3) Candidate locations selection from previous analysis considering maximum stress variation criterion.

As described previously, this work fits in a larger framework for real-time system health evaluation. Future developments will include a more detailed behavior modeling, possibly using an FSI (Fluid Structure Interaction) approach.

The thermal compensation problem will also need to be properly analyzed and addressed.

Finally, the creation of a large dataset will be necessary to train a neural network, which is in this case the surrogate model, to allow the estimation of aileron hinge moment in the real-time process using live data.

Acknowledgement

The authors would like to thank Emanuele Frediani, Francesco Belelli and ICARUS students team at Politecnico di Torino for their continous support in this research activity.

References

Belelli, F. (2020). *Valutazione degli angoli di alettone necessari al compimento di manovre tipiche del profilo di missione di un velivolo*. Politecnico di Torino. Bachelor of Science Thesis.

Berri, P. C., C. Corsi, M. D. Dalla Vedova, A. D. Laudani, P. Maggiore, and C. Secci (2020). Study of packaging and installation of FBG sensors for monitoring of aircraft systems. In *Proceedings of the 30th European Safety and Reliability Conference and the 15th Probabilistic Safety Assessment and Management Conference*. Research Publishing.

Dong, T. and N. H. Kim (2018). Cost-effectiveness of structural health monitoring in fuselage maintenance of the civil aviation industry. *Aerospace 5*(3), 87.

Dupuy, M. J., D. E. Wesely, and C. S. Jenkins (2011). Airline fleet maintenance: Trade-off analysis of alternate aircraft maintenance approaches. In *2011 IEEE Systems and Information Engineering Design Symposium*, pp. 29–34. IEEE.

Frediani, E. (2020). *Studio di una configurazione di sensori ottici per monitoraggio strutturale e applicazioni prognostiche*. Politecnico di Torino. Master of Science Thesis.

Jones, R. M. (1998). *Mechanics of composite materials*. CRC press.

Kamsu-Foguem, B. (2012). Knowledge-based support in non-destructive testing for health monitoring of aircraft structures. *Advanced Engineering Informatics 26*(4), 859–869.

Katz, A. and V. Sankaran (2011). Mesh quality effects on the accuracy of cfd solutions on unstructured meshes. *Journal of Computational Physics 230*(20), 7670–7686.

Ma, Z. and X. Chen (2019). Fiber Bragg Gratings sensors for aircraft wing shape measurement: Recent applications and technical analysis. *Sensors 19*(1), 55.

Melnykowycz, M. M., A. Belloli, P. Ermanni, and M. Barbezat (2006). Integration and reliability of active fiber composite (AFC) sensors/actuators in carbon/epoxy laminates. In *Smart Structures and Materials 2006: Active Materials: Behavior and Mechanics*, Volume 6170, pp. 61701J. International Society for Optics and Photonics.

Qing, X., A. Kumar, C. Zhang, I. F. Gonzalez, G. Guo, and F.-K. Chang (2005). A hybrid piezoelectric/fiber optic diagnostic system for structural health monitoring. *Smart Materials and Structures 14*(3), S98.

Shah, H., S. Mathew, and C. M. Lim (2015). Numerical simulation of flow over an airfoil for small wind turbines using the $\gamma - Re_\theta$ model. *International Journal of Energy and Environmental Engineering 6*(4), 419–429.